Interatomic potentials for the Be–C–H system

C Björkas[1], N Juslin[1], H Timko[1], K Vörtler[1], K Nordlund[1], K Henriksson[2] and P Erhart[3]

[1] EURATOM-Tekes, Department of Physics, University of Helsinki, PO Box 43, FI-00014, Finland
[2] Department of Chemistry, University of Helsinki, PO Box 55, FI-00014, Finland
[3] Lawrence Livermore National Laboratory, Chemistry, Materials, Environmental, and Life Sciences Directorate, L-367, Livermore, CA 94550, USA

E-mail: carolina.bjorkas@helsinki.fi

Abstract

Analytical bond-order potentials for beryllium, beryllium carbide and beryllium hydride are presented. The reactive nature of the formalism makes the potentials suitable for simulations of non-equilibrium processes such as plasma–wall interactions in fusion reactors. The Be and Be–C potentials were fitted to *ab initio* calculations as well as to experimental data of several different atomic configurations and Be–H molecule and defect data were used in determining the Be–H parameter set. Among other tests, sputtering, melting and quenching simulations were performed in order to check the transferability of the potentials. The antifluorite Be_2C structure is well described by the Be–C potential and the hydrocarbon interactions are modelled by the established Brenner potentials.

(Some figures in this article are in colour only in the electronic version)

1. Introduction

One of the objectives of the fusion test reactor ITER is to demonstrate prolonged fusion power production in a deuterium–tritium plasma [1]. The selection of plasma facing materials (PFMs) is a key issue for this objective, and multiple factors have to be taken into account. These include the lifetime of the materials (shortened by erosion and thermal fatigue, for example), safety requirements (tritium retention and activation) and engineering aspects. Due to the ITER tokamak plasma design, the thermal load and particle flux are divided between different areas in the reactor. Consequently, the material requirements vary with location; the current choice for first wall material is beryllium and the diverter region is to be composed of carbon-fibre-composites (CFC) (strike point tiles) and tungsten (baffle and dome) [2, 3].

The choice of Be is motivated by its low Z (which means a lower energy loss due to plasma contamination), its effective oxygen gettering ability and its low tritium inventory. The desirable properties of CFCs are a high melting point, a good thermal shock resistance and an ability to withstand high heat fluxes. The advantages of tungsten, on the other hand, are its low tritium retention and low sputtering yield [3].

The understanding of the retention and recycling of hydrogen isotopes in Be is of particular interest [4], since this will give insight into the undesired trapping of tritium and also into the plasma cooling effect of the release of elements heavier than He.

Another issue that must be understood is the formation of mixed materials, since sputtering and redeposition will unavoidably lead to the creation of surfaces which are made up of a mixture of the three PFMs [5]. The properties of these mixed materials can differ strongly from those of their constituents; hence, predicting their behaviour is considered to be crucial for the reactor operation.

When exploring the consequences of mixed materials and the influence of H isotopes on PFMs, realistic experiments with ITER relevant conditions are preferred but not yet feasible. However, computer simulation is an excellent tool, especially the sub-part of this field, namely the simulation technique based on molecular dynamics (MD), which allows for modelling of tens of millions of atoms. The reliability

of MD is dependent on the accuracy of the interatomic force interactions used in the simulations; hence great efforts must be made in developing proper interaction models, i.e. potentials.

The potential needed for simulating the various processes of interest has to be able to describe variations of the local chemical environment, such as bond-breaking, yet at the same time it must be computationally efficient. Meeting these demands are the so-called analytical bond-order potentials (ABOP), which were initially developed by Tersoff [6] to describe covalent solids but shown by Brenner and Able [7, 8] to be extendable to metals. This potential form has been applied to numerous systems, e.g. to the compound semiconductors Ga–N [9], Ga–As [10], Si–C [11] and Zn–O [11], to the metal–carbon systems Pt–C [8], W–C [12], to hydrocarbons [7] and to the metal Fe [13].

A few potentials for elemental Be already exist, e.g. a cluster potential by Blaisten-Barojas *et al* [14] (here denoted BB), an embedded atom method (EAM) potential by Igarashi *et al* [15] (called IGA), the modified embedded atom method (MEAM) potentials of Baskes *et al* [16] (BAS) and Hu *et al* [17] (HU), and a pure pair potential by Ueda *et al* [18] (U2). But to enable modelling of the whole Be–C–W–H system, potentials compatible with the previously developed W-C–H ones [12] were parametrized in this work. This was done by applying the ABOP formalism on Be, Be–C and Be–H interactions, rendering it possible to join to the earlier C–C and C–H potentials [7, 19]. A Be–W potential will be presented elsewhere.

The paper is organized as follows. In section 2 we describe the potential formalism and how we construct the fitting database (this includes a description of our calculations based on the density functional theory (DFT)) and give a description of the fitting methodology. In section 3 we present and discuss the results of the DFT calculations and of the fitting of each potential (pure Be, Be–C and Be–H separately). In section 4 we present our Be self-sputtering simulations. In section 5 we conclude our work.

2. Method

2.1. Potential formalism

The formalism used originates from the concept of bond order proposed by Pauling [20] and it has been shown [8] to resemble both the tight-binding [21] and the EAM schemes [22, 23]. It has been described extensively elsewhere (in e.g. [8–10]), so only a brief overview will be given in what follows.

The total energy E of the system is expressed as a sum over individual bond energies, as

$$E = \sum_{i>j} f_{ij}^{c}(r_{ij}) \left[V_{ij}^{R}(r_{ij}) - \underbrace{\frac{b_{ij} + b_{ji}}{2}}_{\bar{b}_{ij}} V_{ij}^{A}(r_{ij}) \right]. \quad (1)$$

V_{ij}^{R} and V_{ij}^{A} are the repulsive and attractive terms, respectively.

These are pair potentials of a Morse-like form:

$$V^{R}(r) = \frac{D_0}{S-1} \exp(-\beta\sqrt{2S}(r-r_0)),$$
$$V^{A}(r) = \frac{SD_0}{S-1} \exp(-\beta\sqrt{2/S}(r-r_0)), \quad (2)$$

where D_0 and r_0 are the bond energy and length of the dimer molecule, respectively, and S is an adjustable parameter. β is also related to the dimer, since this can be determined from its ground state oscillation frequency, according to

$$\beta = k \frac{2\pi c}{\sqrt{2D_0/\mu}}, \quad (3)$$

where k is the wavenumber and μ the reduced mass of the dimer.

Through the cutoff function f_{ij}^{c} the interaction range is restricted:

$$f^{c}(r) = \begin{cases} 1, & r \leqslant R - D, \\ \frac{1}{2} - \frac{1}{2}\sin\left(\frac{\pi}{2}(r-R)/D\right), & |R-r| \leqslant D, \\ 0, & r \geqslant R + D. \end{cases} \quad (4)$$

Here, R and D are parameters determining the cutoff range and interval. b_{ij} in equation (1) is the bond-order term, which includes three-body interactions and angularity,

$$b_{ij} = (1 + \chi_{ij})^{-\frac{1}{2}}, \quad (5)$$

where,

$$\chi_{ij} = \sum_{k(\neq i,j)} f_{ik}^{c}(r_{ik}) g_{ik}(\theta_{ijk}) \omega_{ijk} e^{2\alpha_{ijk}(r_{ij}-r_{ik})}. \quad (6)$$

α_{ijk}, ω_{ijk} and θ_{ijk} are fitting parameters. α_{ijk} corresponds to the $2\mu_{ik}$ parameter of earlier potentials [8, 10, 9], and ω_{ijk} is added to make the hydrocarbon potential of Brenner compatible with the present formalism, an approach also adopted in [12]. The angular function g_{ik} is of the form

$$g(\theta) = \gamma\left(1 + \frac{c^2}{d^2} - \frac{c^2}{d^2 + (h + \cos\theta)^2}\right), \quad (7)$$

where γ, c, d and h are adjustable parameters.

2.2. Constructing the fitting database

Filling the fitting database with properties of the Be equilibrium structure is easy, since the available experimental data on hexagonally close-packed (hcp) Be are comprehensive. Experimental data on Be–C are, on the other hand, very scarce due to its chemical instability, and to our knowledge no Be–C phase diagram exists. Moreover, to ensure that a potential is transferable, the fitting database has to cover structures of different atomic coordinations. For these reasons, *ab initio* calculations of several Be and Be–C structures were carried out within the DFT framework. The database was constructed to include cohesive energies, lattice constants, bulk moduli,

pressure derivatives of the bulk modulus, and also elastic constants for the ground state structures.

The DFT calculations used the projector augmented wave (PAW) method [24] in a plane-wave basis set as implemented in the Vienna *ab initio* simulation package (VASP) [25–29]. Pseudopotentials employing the local density approximation (LDA) with the Ceperley–Alder exchange correlation as parametrized by Perdew and Zunger [30], and the generalized gradient approximation (GGA) corrections developed by Perdew and Wang [31, 32] were used. These were taken from the database supplied with VASP. In the metallic pseudopotentials for Be the s and p states, respectively, were treated as valence states.

The sampling of k points in the Brillouin zone was done with the Monkhorst–Pack scheme [33]. The integration over the Brillouin zone was carried out with the linear tetrahedron method of Blöchl *et al* [34].

The calculations for the Be dimer used a supercell with a border length of 13 Å. The energy cutoff for the plane waves was 310 eV. In the calculations of bulk-like Be structures the energy cutoff was 400 eV, except for diamond where 500 eV was used. In most cases $11 \times 11 \times 11$ k points were used. For the hcp and graphene lattices (the latter with a fixed interplanar separation of 10 Å) a finer grid of at least $13 \times 13 \times 13$ k points was used. In these cases the reciprocal lattice was centred on the Γ point. The geometries as well as the internal degrees of freedom were always fully relaxed. The calculations used an accuracy of the order of 10^{-5} eV = 0.01 meV/atom.

In the Be–C case, properties of the theoretical stoichiometric Be–C structures B1 (NaCl), B2 (CsCl) and the zinc blende (ZnS), as well as for the dimer and the only experimentally observed phase, the antifluorite Be_2C phase, were calculated. The calculations for the dimer used a supercell with a border length of 11 Å. The energy cutoff for the plane waves was 400 eV. In the calculations of bulk-like structures the energy cutoff was 700 eV, and $15 \times 15 \times 15$ k points were used. Again, the geometries as well as the internal degrees of freedom were always fully relaxed and the calculations used an accuracy of the order of 10^{-4} eV = 0.1 meV/atom.

To further test the potentials we derived the phonon dispersion curves for hcp-Be in the harmonic approximation. The same methods as when constructing the fitting database were used, i.e. the calculations were carried out within the GGA using the PAW method as implemented in the VASP package. The phonon dispersion curves were obtained using the method of finite displacements and the PHON code for post-processing [35]. For hcp-Be (and also for antifluorite Be_2C) the force constant matrix was computed using a $5 \times 5 \times 5$ supercell, a $5 \times 5 \times 5$ Γ-centred k-point mesh and a plane-wave cutoff energy of 390 eV.

2.3. Fitting methodology

The following general methodology was adopted when fitting a potential. Once an extensive fitting database was constructed, a search for potential parameters that reproduce as many properties as possible was started. When a satisfactory set was found, the potential was tested against properties not included

in the fitting (for instance defect properties and melting point), and if not performing adequately, a new parameter set was investigated. Several iterations were often necessary and compromises were unavoidable.

2.3.1. Beryllium. At ambient conditions beryllium is a metal with a hcp structure. The value of its c/a-ratio is much smaller than the ideal hcp one, 1.5677 compared to 1.63 [36]. At high pressures and at zero pressures just before melting it is seen to transform into the body centred cubic structure [37, 38]. *Ab initio* calculations also suggest that a face centred cubic (fcc) phase exists at high temperatures and pressures [39].

If the interactions are restricted only to nearest neighbours, the energy per bond, E_b, as a function of the equilibrium bonding r_b distance follows the Pauling relation

$$E_b = -D_0 \, e^{-\beta\sqrt{2S}(r_b - r_0)}, \tag{8}$$

with the same parameters as described in section 2.1. This means that the dimer is always the most strongly bonded and has the shortest bond length, and higher coordinated structures have weaker bonds. However, owing to its completely filled subshells ($1s^2 2s^2$), the beryllium dimer is very loosely bound and has a very large bond length and cannot be included in this fitting scheme. Therefore, the β parameter could not be determined from (3) but instead was fitted together with the parameter S to the slope of the Pauling relation from the other phases.

According to our DFT calculations, the body centred cubic (bcc) structure (which has eight nearest neighbours, $Z = 8$) does not follow this relation either, since its energy per bond is higher than the energy per bond of the simple cubic (sc) structure ($Z = 6$). In order to account for this behaviour, second nearest neighbour (2nn) interactions were allowed when fitting the bcc structure. This also helps to prevent problems related to a steep cutoff, since the difference between the bcc first nearest neighbour (1nn) and 2nn distance is only about 14%.

Two different Be parameter sets were developed. The first set, Be–Be I, was constructed for pure Be interactions, whereas the second one, Be–Be II, describes the Be–Be interactions when used together with the Be–C potential. The different parameter sets are found in table 1, together with the Be–C, Be–H and hydrocarbon sets.

2.3.2. Be–C. Only one intermediate phase of beryllium carbon has been reported [36]. This Be_2C is ionic and its structure is cubic antifluorite, which can be described as carbon atoms occupying fcc sites and beryllium atoms forming a cubic sublattice inside. In this way, each C atom is surrounded by eight Be atoms. The distance between the closest Be atoms is only $a_0/2$, which made it impossible to fit Be–Be and Be–C interactions independently. The potential fitted to pure Be (Be–Be I) was not suitable as such for Be–Be interactions in Be_2C; hence, a second Be version (Be–Be II) was constructed as mentioned above. With this version, properties such as the cohesive energy of hcp-Be could not be exactly reproduced.

The few experiments focusing on Be_2C have determined its structural and electronic properties, but as far as other

Table 1. Parameter sets for the different interaction types. The Be–Be II set is to be used together with the Be–C potential. The C–C, H–H, H–C and C–H sets are taken from [7]. The α_{ijk} parameter is zero except for the hydrocarbons for which it equals $\alpha = 4.0$, (but $\alpha_{CCC} = 0$) and $\alpha_{BeBeBe} = 0.85$ within the Be–Be I potential. $\omega_{CCH} = 0.339\,46$, $\omega_{CHC} = 2.945\,86$, $\omega_{HHC} = 4.544\,15$, $\omega_{HCH} = 0.220\,06$ and all other $\omega = 1.0$.

	Be–Be I	Be–Be II	C–C	H–H	Be–C	Be–H I	Be–H II	H–C	C–H
D_0 (eV)	1.17	1.035 71	6.0	4.7509	3.909 3330	2.6	2.6	3.642	3.6422
r_0 (Å)	2.035	2.078 80	1.39	0.741 44	1.724 299	1.338	1.338	1.1199	1.1199
β (Å^{-1})	1.28	1.3	2.1	1.9436	1.586 761	2.3	2.2	1.9583	1.9583
S	3.111 67	1.889 82	1.22	2.3432	2.766 724	3.0	2.5	1.690 77	1.690 77
γ	$4.787\,01 \times 10^{-7}$	$8.195\,87 \times 10^{-7}$	2.0813×10^{-4}	12.33	$3.001\,84 \times 10^{-5}$	0.14	0.19	12.33	2.0813×10^{-4}
c	32.327 97	89.3894	330.0	0.0	57.004 094	0.0057	0.0057	0.0	330.0
d	0.052 65	0.274 43	3.5	1.0	0.358 304	0.002	0.004	1.0	3.5
h	0.826 579 99	0.760 6934	1.0	1.0	0.559 9960	1.0	1.0	1.0	1.0
R (Å)	2.685	2.535	1.85	1.40	2.60	1.75	1.80	1.55	1.55
D (Å)	0.223	0.15	0.15	0.30	0.20	0.15	0.15	0.25	0.25

properties (for instance binding and elastic features) are concerned they have only been able to conclude that it has a high melting temperature ($\sim$2670 K [36]) and that its bulk modulus is slightly larger than that of SiC ($B = 233$ GPa) [40]. Given this situation, proper testing of the transferability of the potential against experiments cannot be done, and the fitting database mainly comprises values obtained using our own DFT calculations.

Second nearest neighbour interactions, i.e. Be–Be interactions, were included in the CsCl structure as well as in the antifluorite structure. This means that, in principle, one could fit the Be–C potential so as to reproduce the Be–C structures with only 1nn interactions first, and then tune the pure Be potential to get the antifluorite and CsCl structures correct. The fitting was, however, done simultaneously for both parameter sets and it turned out to be quite difficult to preserve the good features of Be–Be I while at the same time trying to get a decent Be–C potential.

The short-ranged character of the ABOP scheme could also add to the difficulties of encapsulating ionic interactions that are long-ranged, but it has been shown by extensive testing that the ABOP formalism is adequate for mimicking ionic systems such as gallium nitride even without additional long-range or charge-transfer terms [41].

2.3.3. Be–H. As we had to construct two different Be–Be potentials, we also constructed a Be–H potential for each of them. For a Be–H potential intended for bombardment simulation several aspects need to be considered. After the incident hydrogen has entered the bulk of the Be, the energetics and the geometry of the movement of the incident atom and the defect structures it ends up in are most important, as studied by Krimmel and Fähnle [42] and Ganchenkova *et al* [43]. The interaction with other defects, accumulation of hydrogen and surface effects are of course of interest but have not been studied much in the literature. Small Be–H molecules, which determine the forms of the sputtered species, were studied using DFT by Allouche [44]. We fitted the potential to data for Be–H$_n$-molecules and to energetics of the single H interstitial in Be.

3. Results and discussion

3.1. Beryllium

3.1.1. DFT data. The properties of the Be dimer as obtained from the GGA DFT calculations are found in table 2. The same table also includes the results of bulk property calculations of Be in the diamond, fcc, bcc and the ground state structure hcp.

When compared to experimental values, the dimer bond length and its vibration frequency are well reproduced. We did not, however, reproduce the weak low temperature bond strength, which is a problem also encountered in other DFT calculations (e.g. [45, 46]).

The experimental properties of hcp-Be are closely reproduced, the only exception being the cohesive energy, which the DFT calculations overestimate when compared to experimental values. The GGA overestimation was 0.39 eV and the LDA 0.88 eV. Due to this, the cohesive energies of all phases were modified before including them in the fitting database. This was done by adding the calculated energy differences relative to the hcp phase, $E_{coh,calc}^i - E_{coh,calc}^{hcp}$, to the experimental value of $E_{coh,exp}^{hcp} = 3.32$ eV/atom. The motivation behind shifting the energies of all phases stems from the fact that although DFT calculations of cohesive energies are known to be subject to systematic errors, the energy differences are usually correct. A similar correction was made to the lattice constants, where each constant was scaled with the factor $V_{DFT}^{hcp}/V_{Exp}^{hcp}$. No modification was made to the dimer properties, since we did not make any attempt to fit the dimer.

3.1.2. Fitted properties. Figure 1 is an illustration of the agreement between the analytical potentials and the reference data. The bcc and hcp phases deviate from the straight line corresponding to the Pauling relation, equation (8), since 2nn interactions were included in the bcc calculations and two different bond lengths (one for the six basal neighbours and one for the six non-basal ones) were considered in the hcp structure. The difference stems from the non-ideal c/a ratio. An overall good agreement between the Be–Be I potential (circles) for all the phases is found, but neither the dimer bond length nor its strength could be reproduced.

Table 2. Properties of the beryllium dimer and bulk phases (both hypothetical and existing ones) as obtained from experiments, DFT calculations and using the analytical potentials derived in this work. For the hexagonal close-packed structure, also values obtained with literature potentials are included. (For the potentials found in [14, 16, 17], only available reported values are added). The notation is as follows: ω_e, vibration frequency; r_0, bond length; E_{coh}, cohesive energy; a, lattice parameter; V_0, atomic volume; B, bulk modulus; B', pressure derivative of the bulk modulus. For the DFT calculations in this work, shifted values for E_{coh} and r_0 are given (see text).

		DFT		ABOP		Other potentials				
	Experiment	Others	This work	Be–Be I	Be–Be II	BB [14]	IGA [15]	BAS [16]	HU [17]	U2 [18]
Dimer Be$_2$										
r_0 (Å)	2.45[a]	2.45[b]	2.43	2.04	2.08					
E_{coh} (eV/atom)	−0.05 (77 K)[a], −0.31 (298 K)[c]	−0.21[b]	−0.23	−0.59	−0.52					
ω_e (cm^{-1})	275.8[a]	244.0[b]	245	481	459					
Graphite (gra, A9, $P6_3/mmc$, no. 194)										
a (Å)			2.14	2.10	2.11					
E_{coh} (eV/atom)			−1.25	−1.41	−1.43					
B (GPa)			—	1.73	1.81					
B'			—	3.99	3.75					
Diamond (dia, A4, $Fd\bar{3}m$, no. 227)										
a (Å)			4.94	4.93	4.97					
E_{coh} (eV/atom)			−1.73	−1.71	−1.73					
B (GPa)			45.1	30.3	31.4					
B'			3.68	4.00	3.74					
Simple cubic (sc, A$_h$, $Pm\bar{3}m$, no. 221)										
a (Å)			2.20	2.18	2.20					
E_{coh} (eV/atom)			−2.33	−2.31	−2.27					
B (GPa)			75.7	58.8	61.9					
B'			3.24	4.08	3.81					
Body centred cubic (bcc, A2, $Im\bar{3}m$, no. 229)										
a (Å)	2.55 (1523 K)[d]		2.48	2.50	2.42					
E_{coh} (eV/atom)			−3.22	−3.27	−3.58					
B (GPa)		109.5[e]	127.2	335.3	934.9					
B'			3.41	−1.64	6.86					
Face centred cubic (fcc, A1, $Fm\bar{3}m$, no. 225)										
a (Å)			3.18	3.23	3.25					
E_{coh} (eV/atom)			−3.24	−3.16	−3.56					
B (GPa)		107.6[e]	123.8	114.3	132.1					
B'			3.45	4.15	3.87					
Hexagonal close-packed (hcp, A3, $P6_3/mmc$, no. 194)										
a (Å)	2.2856 (293 K)[d]	2.27[e]	2.289	2.30	2.32	2.25	2.285	2.278	2.289	2.26
c/a	1.5677 (293 K)[d]	1.573[e]	1.566	1.572	1.558	1.633	1.571	1.568	1.568	1.64
E_{coh} (eV/atom)	−3.32[f], −3.36[a]	−3.60[g]	−3.32	−3.32	−3.62	−3.60	−3.31	−3.43	−3.32	−3.24
V_0 (Å^3/atom)	8.11 (293 K)[d]	7.92[e]	7.93	8.27	8.52	8.05	8.12	8.03	8.14	8.20
B (GPa)	109.88[h], 116.8[i]	122[e]	126.3	120.2	134.4	—	137.5	111.7	—	263.8
B'	3.584[h], 4.6[j]	3.306[e]	3.31	4.16	3.88	—	0.46	—	—	3.12

[a] Reference [70]. [b] Reference [46]. [c] Reference [71]. [d] Reference [36]. [e] Reference [39]. The bulk moduli for bcc and fcc are determined from the relation $B = (c_{11} + 2c_{12})/3$. [f] Reference [72]. [g] Reference [73]. [h] Reference [37]. [i] Reference [74]. [j] Reference [75].

The same comparison can be done with the Be–Be II potential (squares in figure 1), resulting in a somewhat poorer agreement. All the cohesive energies except for that of the diamond and sc phases are now overestimated and similar to the values obtained from the DFT calculations (table 2). This overshooting was, however, necessary to get a good Be–C potential.

Additional Be bulk properties as predicted by the two ABOP potentials are found in table 2, which also illuminates the better performance of Be–Be I. The bulk modulus and its pressure derivative agree with the reference data for almost all phases, the only exception being the bcc phase for which the modulus is more than twice as large within Be–Be I. Be–Be II predicts an even higher value. The Be–Be I version of the potential shows a negative value for the pressure derivative of the modulus, although the DFT calculations indicate otherwise. Also included in the table are values as given by the literature Be potentials. The MEAM potentials BAS and HU, as well as BB, could not be easily implemented in the same code as the other potentials, and hence we restrict the comparison with those to the values reported in the literature.

Table 3. Elastic constants of hexagonal close-packed Be. Values obtained in experiments, with DFT calculations and by using the analytical potentials derived in this work are included.

	Experiment		DFT		ABOP	
	Ref. [39]	Ref. [74]	Ref. [75]	This work	Be–Be I	Be–Be II
c_{11} (GPa)	293.6	295.4	300.8	302.7	280.5	233.6
c_{12} (GPa)	26.8	25.9	14.1	29.4	58.6	83.0
c_{13} (GPa)	14.0	−1.0	7.1	16	13.5	82.1
c_{33} (GPa)	356.7	356.1	359.5	368	349.7	248.0
c_{44} (GPa)	166.2	170.6	160.2	166.9	198.2	175.4
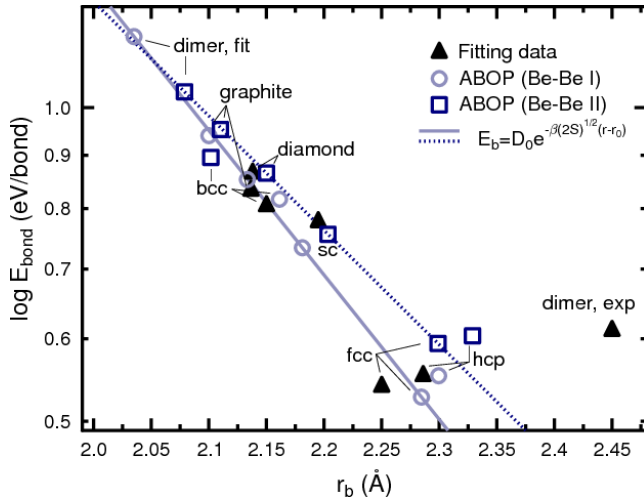
Figure 1. Semilogarithmic plot of the energy–bond relation for different beryllium phases. The fitting data are scaled DFT data (see text). The scaling was done in order to fit the ground structure hcp to experimental properties. The circles show values predicted by the bond-order potential (ABOP) Be–Be I, the squares are the Be–Be II potential, and the lines are the Pauling relation with parameters of each version.

Figure 2. The volumetric thermal expansion of Be and Be_2C.

The most important structure is hcp, which retains its status as the ground state structure in both potentials of this work. The c/a ratio is, as is should be, smaller than the ideal one of $\sqrt{8/3} \approx 1.63$ and the bulk moduli are within reasonable limits from the experimental values. Contrary to the other literature Be potentials, the pair potential U2 cannot reproduce the small c/a ratio and overestimates the bulk modulus.

The calculated Be elastic constants are shown in table 3. Be–Be I is seen to reproduce them excellently, whereas the deviations are slightly larger within Be–Be II.

3.1.3. Tested properties. The melting temperature was determined by simulating a solid–liquid interface at zero pressure and different temperatures [47]. The melting temperature was defined as the temperature at which the system was in equilibrium, i.e. when the fractions of solid and liquid parts remained constant. The simulations were performed with a simulation cell of 1800 atoms for 50 ps. Potential Be–Be I predicts a melting temperature of 1550 ± 50 K, which agrees well with the experimental value of 1560 K. The melting point within Be–Be II is higher, about 2600 ± 50 K. In U2, the melting point was also estimated to 2600 ± 50 K and in IGA 2150 ± 50 K.
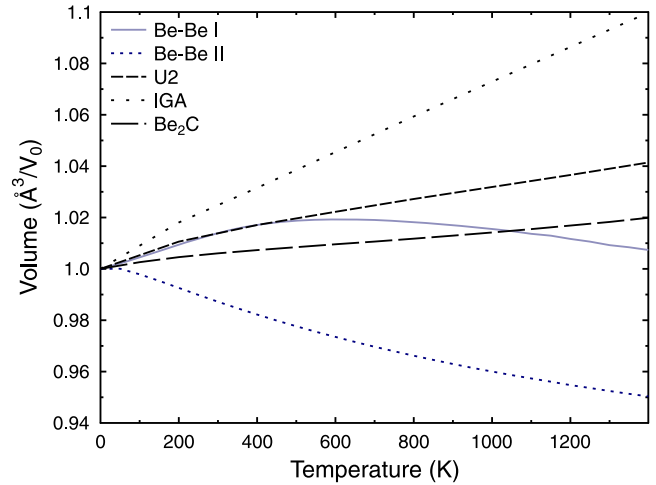
Figure 4 illustrates the 300 K isotherm of hcp-Be with both Be–Be I and Be–Be II as compared to two experiments [48, 49] and DFT calculations [39]. The isotherm of Be–Be II follows the shock-wave experiment of Nakano *et al* [48] (Exp. 1 in the figure) at low pressures and the compressibility within Be–Be I lies between the two experiments at all pressures.

When heated, Be exhibits a non-monotonic volumetric expansion (see figure 2). According to Be–Be I, Be expands until about 500 K, when it compresses at the same rate until melting. A negative volumetric thermal expansion is seen at all temperatures for Be–Be II. Contrary to experimental observations (e.g. [50]), the c/a ratio increases with temperature in both versions, although the two dimensions (perpendicular and parallel to the (0001)-axis) behave anisotropically: in Be–Be I the perpendicular axis increases and compresses in the same way as the volume, whereas the parallel dimension increases at all temperatures. In Be–Be II it is the c-axis that expands non-monotonically: it grows until 300 K when it starts to diminish. The a-axis, on the other hand, diminishes as a function of temperature. The expansion coefficients are found in table 5, where they are compared to experimental values and estimations using other Be potentials.

Point defect formation energies and binding energies for the ABOPs are found in table 6. The formation energies were calculated according to
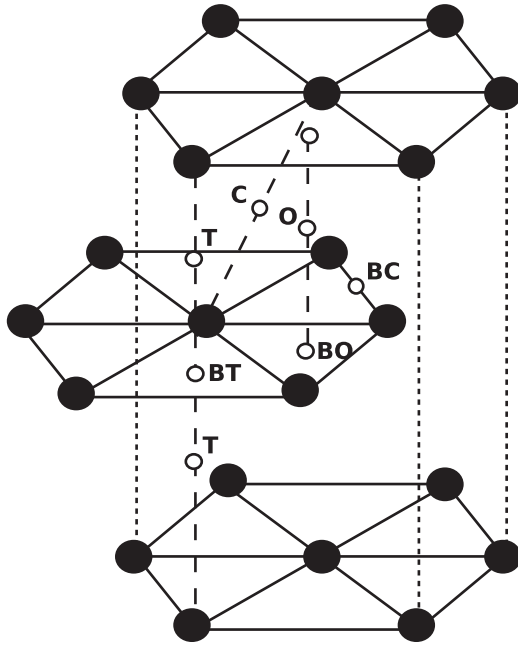
$$E_f = E_{def}(N) - N E_{coh}, \qquad (9)$$

Figure 3. High symmetry interstitial positions in the hexagonal lattice. T stands for tetrahedral, O for octahedral, C for crowdion, and BT, BO and BC for the corresponding basal positions. The split and basal split configurations have been left out for reasons of clarity.

Figure 4. The 300 K isotherm of Be as predicted by the two potentials of this work, by DFT calculations of [39] and by two experiments. Exp. 1 is from [48] and Exp. 2 (room temperature) is from [49].

where $E_{def}(N)$ is the energy of the cell with a total of N atoms including the defect (interstitial or vacancy) and E_{coh} is the energy of one atom in a perfect cell. The divacancy binding energies were estimated through

$$E_b = 2E_f^s - E_f^{divac}, \qquad (10)$$

where E_f^s and E_f^{divac} are the formation energy of a single vacancy and a divacancy, respectively. The simulations were done at zero pressure and 0 K.

Several different interstitial configurations were studied (see figure 3 for an illustration of the positions), but only a couple of them (basal octahedral (BO) and crowdion (C)) are stable for the potentials in this work, BO being the most stable. Hence, both the ABOP potentials have the right ground state interstitial configuration when compared to the DFT calculations of Ganchenkova *et al* [43]. However, these calculations indicate that all but the basal crowdion (BC) and basal tetrahedral (BT) configurations are stable.

The most stable interstitial configuration in the IGA potential is the C structure, which has a large formation energy (8 eV). As pointed out in [15], the absolute values for the interstitials are governed by interactions at short ranges, and since this potential was not fitted for such conditions, the formation energies are not expected to be reasonable. A short-range addition for the potential could change the situation. The pair potential U2, on the other hand, does surprisingly well in describing the interstitials when compared to DFT calculations, since it predicts the BO to be the most stable with a formation energy of 5.10 eV. In the HU potential, the only stable configuration is BS, with a formation energy of 2.96 eV [17].

When looking at the vacancy energetics, disagreements with the DFT results and the ABOPs are found. The
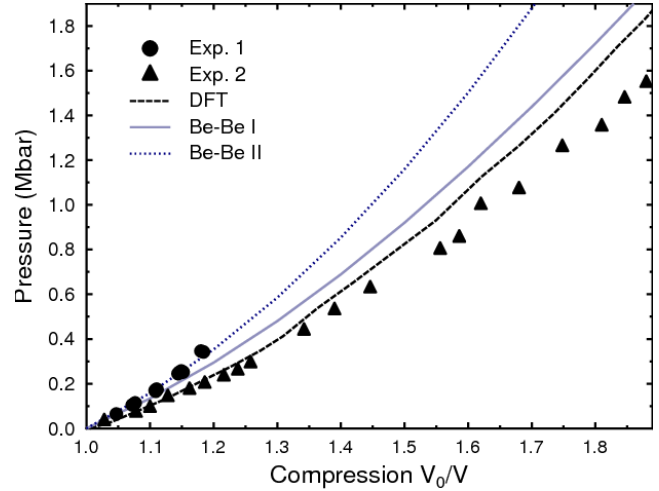
ABOPs cannot reproduce the low DFT formation energy of a single vacancy nor the different (in plane and out of plane configurations) divacancy ones. (The experimental value for the vacancy formation is, however, not clearly determined, see e.g. [51] for a discussion.) Moreover, contrary to the same calculations, the divacancies are stable, although they have a very small binding energy.

The divacancy binding energies are also positive within all the other Be potentials (IGA, BAS, HU and U2). A vacancy formation energy of 1.13 eV has been used in the fitting of these potentials, the exception being the U2 potential, where this energy is calculated to be 3.10 eV. In U2, the divacancy binding energies are 5.89 and 5.83 eV for the in-plane and out-of-plane divacancies, respectively, which is about three times larger than the corresponding DFT values.

The mobility activation of a self-interstitial atom (SIA) in Be was calculated by following the mean square displacement $\langle R^2 \rangle$ for $t = 10$ ns and then calculating the diffusivity D using the atomistic definition $\langle R^2 \rangle = 6Dt$. An Arrhenius fit was made to the diffusivity data to obtain the activation energy. The diffusion simulations were done in a cell with constant volume (the equilibrium lattice constant at each temperature was used), and the temperature was controlled only during the first 50 ps of the runs. The temperature range was 500–1100 K. The energies and diffusion prefactors were $E_A^I = 0.72 \pm 0.01$ eV, $D_0^I = (9.6 \pm 0.6) \times 10^{-2}$ cm^2 s^{-1} and $E_A^{II} = 0.73 \pm 0.01$ eV, $D_0^{II} = (7.6 \pm 0.4) \times 10^{-3}$ cm^2 s^{-1} for Be–Be I and Be–Be II, respectively.

Table 7 shows surface energies, including available DFT values. The energies were calculated following the method of [52], i.e. $\sigma_i = (E^{bulk} - E_i^{surf})/N_{surf}/2$, where i is the surface of interest, E^{bulk} is the total energy of the simulation cell with periodic boundaries, E_i^{surf} is the energy of the cell with open surfaces and N_{surf} is the number of surface atoms. The total number of atoms used in these simulations was 3072.

Both ABOP potentials are seen to agree with the DFT values for the (0001) surface. Although no values for the other
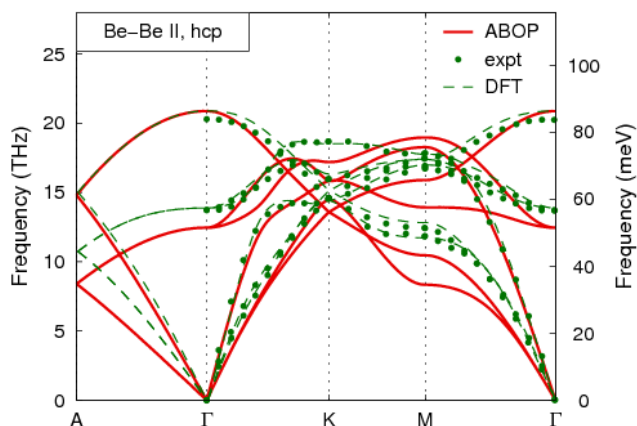
Figure 5. The phonon dispersion curves for hcp-Be according to DFT calculations, experiments [53] and the Be–Be II potential.

surfaces exist for comparison, the ABOP predictions can be considered realistic since both ($1\bar{1}00$) and ($2\bar{1}00$) surfaces are higher in energy than the close-packed (0001) surface. The other Be potentials also give reasonable values, but the energy of the (0001) surface in the IGA potential is slightly negative.

The results of the phonon dispersion calculations are shown in figure 5 in comparison with experimental [53] and DFT results. The overall agreement is good with the biggest deviations on the order of 2 THz at the M-point.

3.2. Be–C

3.2.1. DFT data.
The results of the Be–C calculations are found in table 4 together with the dimer properties. As opposed to the pure Be case, the calculated cohesive energy of Be_2C is not overestimated when compared to the experimental values, although the experimental uncertainties are large. An excellent agreement with the lattice constant is also seen. But, due to a lack of data, no other comparisons to experimental values can be done. Similarities are, however, found when comparing the bulk modulus of Be_2C and its pressure derivative with earlier DFT calculations. Our calculations also show that the antifluorite phase is the only structure out of several different ones (CsCl, NaCl, ZnS, $L1_0$, $L1_2$—both Be_3C and BeC_3) with a negative formation energy. This is line with the fact no phase other than the antifluorite one has been observed.

3.2.2. Fitted properties.
How well the ABOP reproduces the reference data of different phases can be seen in table 4. The absence of experimental data and the few literature *ab initio* data clearly illustrate the difficulty of assessing the Be–C potential behaviour. Many difficulties were found when fitting the antifluorite structure, and a good Be–C fit to the reference data was obtainable only at the expense of an acceptable Be potential.

With this potential, the antifluorite structure is the most stable structure against mixing, its bulk modulus and pressure derivative agree well with the calculated values, and the elastic constants are of the right order. It was, however, not possible to reproduce exact values of the elastic constants. The lattice

constant is also slightly larger than the experimental value, and the cohesive energy is somewhat smaller. Experimental values for the cohesive energy can be obtained by considering the measured values of the heat of formation of Be_2C (-92.5 ± 15.7 kJ mol^{-1} [54] and -117.2 kJ mol^{-1} [55]) and the cohesive energy of the constituents. With the two different heat values, we arrive at energies of -16.8 ± 0.6 and -17.55 eV/f.u., which suggests that the ABOP (-16.02 eV/f.u.) only makes a small underestimation of 2–9%. (See appendix B for details of the calculation of the formation energy.)

The NaCl structure is not stable in this potential, but reconstructs into a crystal with positive formation enthalpy. Likewise, the ZnS structure relaxes into a deformed structure (containing grain boundaries) with a small, but positive, formation energy. As in the DFT calculations, we checked several other crystal structures as well, but only the Be_2C structure showed a negative formation enthalpy according to the ABOP.

3.2.3. Tested properties.
The melting point of Be_2C was determined following the same procedure as in the beryllium case (see section 3.1.3). A simulation cell of 1596 atoms was used. The resulting melting temperature of 3200 ± 50 K agrees fairly well with the observed one of 2670 K [36].

Be_2C expands thermally at a rate of 4.5×10^{-6} K^{-1}, which is in quite good agreement with the experimental value of 5.8×10^{-6} K^{-1} [56].

A check whether any spurious minima exist was done by slowly quenching a simulation cell containing completely molten Be_2C (4096 Be and 2048 C atoms) or randomly distributed atoms. The latter cell was constructed by randomly placing 6144 Be and C atoms (ratio 2:1) in a cube of side length 60 Å. Different runs were performed, with cell temperatures starting from well above the melting temperature and gradually being cooled down to 0 K at a rate of 2–10×10^{-4} K fs^{-1}. The temperature was held at 4000 K for 20 ps to ensure random positions of the melt. When a temperature of about 2500 K was reached, a phase transition was observed in all cases. This transition is observed as a sudden drop in the total energy, which is plotted as a function of the simulation time in figure 6. As seen, the antifluorite structure was eventually reached independently of the cooling rate. A few defects or stacking faults remained in the simulations (see figure 7(b)), explaining the differences in the final energies of the quenched cells and the ideal cohesive energy in figure 6. The time evolution of the radial distribution function for cooling a random distribution at a rate of 0.001 fs K^{-1} is found in figure 8. In this case, the antifluorite phase transition takes place after about 2 ns.

We also noted that on quenching stoichiometric BeC, the melt is segregated into regions of amorphous three-fold coordinated C and Be_2C (see figure 7(c)).

The vacancy formation energies of Be_2C were calculated following the method described in appendix B, resulting in a Be vacancy formation energy of 0.73 eV and a C vacancy formation energy of 3.40 eV.

The phonon dispersion curve for Be_2C as obtained from the ABOP is shown in figure 9 in comparison with results from

Table 4. Properties of the Be–C dimer and bulk phases (including hypothetical ones) as obtained from experiments, DFT calculations and using the analytical potential (ABOP) derived in this work. The two different values taken from [76] correspond to different DFT calculations. The notation is as follows: ω_e, vibration frequency; r_0, bond length; E_{coh}, cohesive energy; E_f, formation energy; a, lattice parameter; V_0, atomic volume; B, bulk modulus; B', pressure derivative of the bulk modulus; c_{ij}, elastic constants.

| | | DFT | | | |
	Experiment	Ref. [76]	Ref. [77]	This work	ABOP
Dimer BeC					
r_0 (Å)				1.68	1.72
E_{coh} (eV/f.u.)				−2.94	−3.90
ω_e (cm^{-1})				582	1020
L1$_0$ ($P4/mmm$, no. 123)					
a (Å)				2.22	2.38
c/a				1.24	1.41
E_{coh} (eV/f.u.)				−10.10	−10.62
E_f (eV/f.u.)				2.72	0.38
B (GPa)				172.5	1060.5
B'				3.59	2.81
Be$_3$C (L1$_2$, $Pm\bar{3}m$, no. 221)					
a (Å)				3.00	3.09
E_{coh} (eV/f.u.)				−18.14	−18.00
E_f (eV/f.u.)				2.13	0.24
B (GPa)				163.6	220.3
B'				3.75	4.33
BeC$_3$ (L1$_2$, $Pm\bar{3}m$, no. 221)					
a (Å)				3.02	2.82
E_{coh} (eV/f.u.)				−19.79	−17.39
E_f (eV/f.u.)				11.20	8.36
B (GPa)				169.426	417.6
B'				3.91	4.94
Zinc blende (ZnS, B3, $F\bar{4}3m$, no. 216)					
a (Å)				4.16	—
E_{coh} (eV/f.u.)				−10.06	—
E_f (eV/f.u.)				2.75	—
B (GPa)				135.4	—
B'				3.43	—
Rock salt (NaCl, B1, $Fm\bar{3}m$, no. 225)					
a (Å)				3.87	—
E_{coh} (eV/f.u.)				−10.41	—
E_f (eV/f.u.)				2.40	—
B (GPa)				181.7	—
B'				3.59	—
Caesium chloride (CsCl, B2, $Pm\bar{3}m$, no. 221)					
a (Å)				2.42	2.38
E_{coh} (eV/f.u.)				−9.93	−10.62
E_f (eV/f.u.)				2.88	0.38
B (GPa)				176.5	341.3
B'				3.38	−0.19
Antifluorite Be$_2$C (C1, $Fm\bar{3}m$, no. 225)					
a (Å)	4.33^a, 4.342^b	4.27, 4.29	4.27	4.33	4.57
E_{coh} (eV/f.u.)	−16.8 ± 0.6^c, −17.55^d	−17.58, −18.09	−18.1	−17.46	−16.02
E_f (eV/f.u.)	−2.9 ± 0.5^e, −1.2^f			−1.39	−1.31
V_0 (Å^3/atom)	6.77^a, 6.82^b	6.49, 6.58	6.49	6.77	7.96
B (GPa)		216, 213	217.74	205.7	227.3
B'		3.5, 4.18	3.63	3.34	4.22
c_{11} (GPa)				438.3	570.1	331.6
c_{12} (GPa)				106.43	15.1	175.2
c_{44} (GPa)				165.95	194.7	204.7

^{a} Reference [78]. ^{b} Reference [79]. ^{c} Obtained with formation energies for Be$_2$C from [54], and for Be and C (graphite) from [55].
^{d} Obtained with formation energies for Be, C (graphite) and Be$_2$C from [55]. ^{e} Reference [54]. ^{f} Reference [55].

Table 5. Room temperature Be thermal expansion coefficients. The linear expansion coefficients for Be are given as perpendicular $\alpha_\perp$ and parallel $\alpha_\parallel$ to the (0001)-axis (in K^{-1}). The volumetric coefficient is expressed as α_V (in K^{-1}). Unless specified, the measurements were done at 300 K.

Be	ABOP		Other potentials		Experiment	
	Be–Be I	Be–Be II	IGA [15]	U2 [18]	Ref. [50]	Ref. [80]
$\alpha_\perp \times 10^6$	4.8	−26.6	21.1	12.8	7.7	12.6
		36.5 (100 K)				
$\alpha_\parallel \times 10^6$	30.0	−1.2	23.4	5.4	10.6	9.1
		−6.0 (500 K)				
$\alpha_V \times 10^6$	38.2	−52.5	65.8	31.9	29.0	
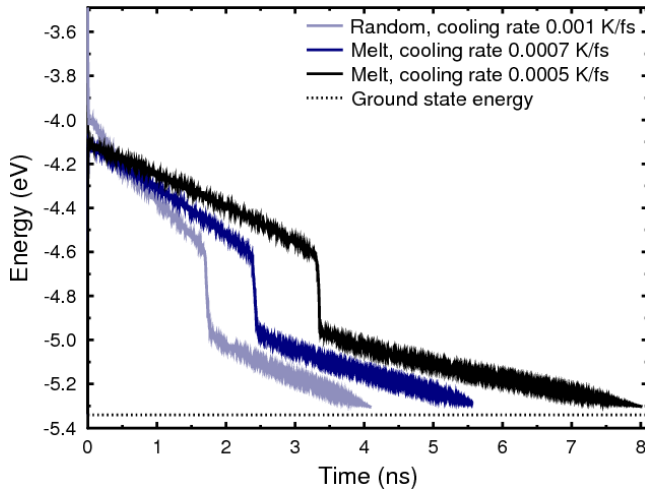
Figure 6. The total energy of Be_2C at temperatures going from 4000 to 0 K with different cooling rates. The phase transition to the antifluorite structure is seen as a sudden drop in the energy. Both a random distribution and melted Be_2C were used as the initial structure.
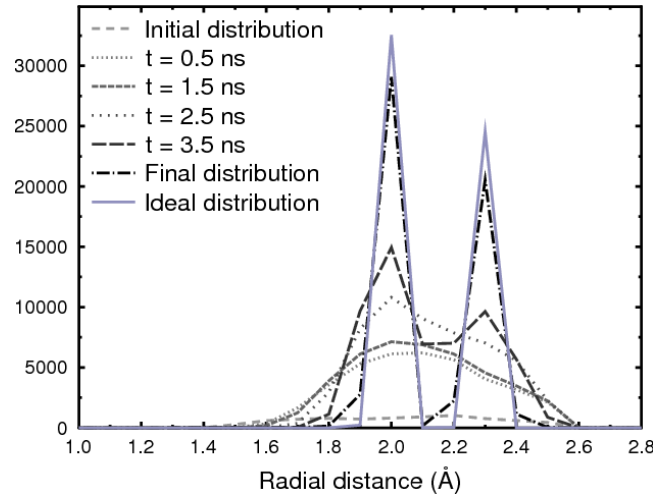

Figure 8. The radial distribution of Be_2C as a function of time, starting from 4096 Be and 2048 randomly distributed atoms. The temperature starts from $T = 4000$ K and goes to 0 K at a rate of 0.001 K fs^{-1}. The first peak corresponds to Be–C nearest neighbours and the second peak is Be–Be neighbours.

our DFT calculations. The agreement is encouraging, although some larger deviations for the optical branches half-way along the Γ–X and Γ–L lines must be acknowledged.

3.3. Be–H

3.3.1. Fitted properties. Certain properties of the molecules given by DFT cannot be reproduced using a Tersoff type

potential, at least without interaction between the hydrogen atoms, which are farther apart than the cutoff of the well established H–H potential we use. For instance, according to DFT, the bond lengths for BeH_2 are smaller than the dimer bond length and larger for BeH_3, which is not possible to reproduce with the Tersoff formalism. The total energy of BeH_2 cannot be larger than $2D_0$, while DFT gives it as $\sim 2.5D_0$. Modifying the formalism to allow for this was,
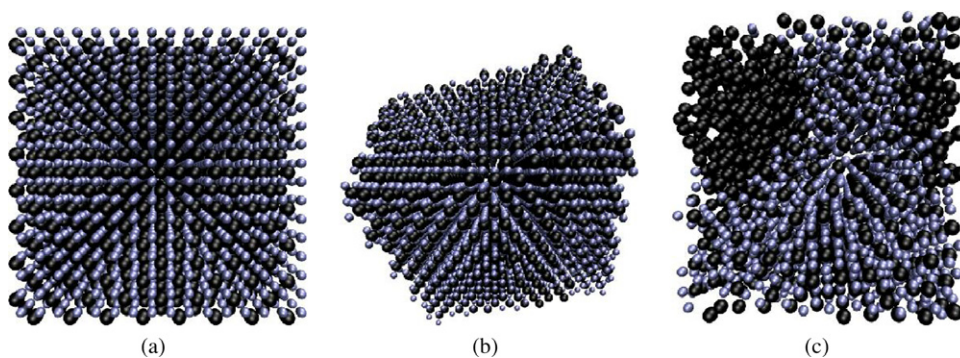

Figure 7. (a) The ideal antifluorite Be_2C structure. (b) The final structure after quenching from $T = 4000$ to 0 K at a rate of 0.5 K ps^{-1} with a ratio Be:C = 2:1 in the initial melt. Both (a) and (b) illustrate the antifluorite structure while (c) shows the final structure after quenching a random melt with Be:C = 1:1. Regions of amorphous three-fold coordinated carbon and Be_2C are seen.

Table 6. Point defect energies in Be as predicted by the two potentials in this work and by DFT calculations. The energies are given in eV. $2V_{AA}$ stands for a divacancy in a basal plane and $2V_{AB}$ for two vacancies out of plane. The studied interstitial configurations are crowdion (C), octahedral (O), split (S), tetrahedral (T), and the corresponding basal ones (indicated with a B). E_f, formation energy in eV; E_b, binding energy in eV.

	ABOP		DFT		
	Be–Be I	Be–Be II	Ref. [43]	Ref. [51]	Ref. [42]
Interstitials					
E_f^C	2.91	2.84	4.39		
E_f^O	Unstable	Unstable	5.24		
E_f^S	Unstable	Unstable	5.29		
E_f^T	Unstable	Unstable	5.22		
E_f^{BC}	Unstable	Unstable	Unstable		
E_f^{BO}	2.55	2.29	4.20		
E_f^{BS}	Unstable	Unstable	4.30		
E_f^{BT}	Unstable	Unstable	Unstable		
Vacancies					
E_f	1.68	2.04		0.81	1.13
$E_f^{2V_{AA}}$	3.19	3.83		1.96	
$E_f^{2V_{AB}}$	3.08	3.80		2.07	
$E_b^{2V_{AA}}$	0.16	0.24	−0.26		
$E_b^{2V_{AB}}$	0.27	0.26	−0.37		

however, not desired, as the binding energies and bond lengths are still acceptable with the formalism used for all other interactions in the Be–C–W–H system.

According to DFT, and reproduced by the Be–Be potentials, the self-interstitial atom in pure beryllium is in the BO position in the ground state (table 6). For interstitial H, DFT gives a different position, BT, also known as the hexahedral position [42, 43, 57]. The positions are shown in figure 3. The calculations by Ganchenkova give a higher formation energy than those by Krimmel, about 1.6 eV and 0.8 eV, respectively, and experiments with tritium give about 1 eV [58].

Finding a parameter set with good formation energies for the BT and octahedral (O) interstitial positions was relatively easy, but the ground state was always an off-plane position above or below the BT position, in the tetrahedral (T) position, or between T and BT. Forcing the potentials to keep the ground state as BT (both in energy and position) led to high migration barriers. The best parameter set to give the correct ground state had a migration barrier of about 3 eV for BT to O migration, which is unacceptably high compared to 0.38 eV according to DFT [43]. Thus we decided to accept that the ground state is in the wrong position in order to keep both the defect energies and migration energies reasonable.

Table 7. Surface energies (in eV/atom) in Be as predicted by the two Be potentials in this work, by literature potentials and by DFT calculations.

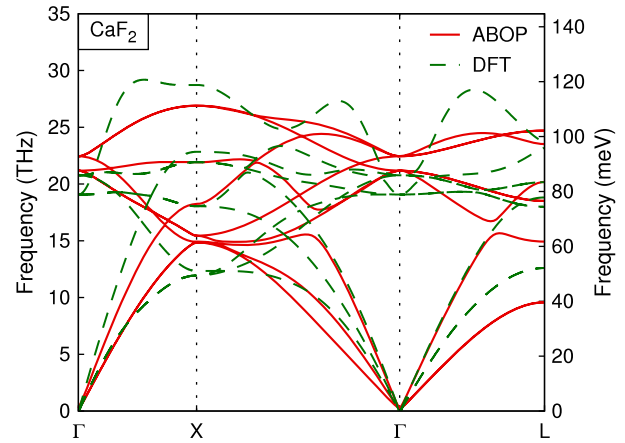|	ABOP		Other potentials				DFT	
Surface	Be–Be I	Be–Be II	IGA [15]	BAS [16]	HU [17]	U2 [18]	Ref. [81]	Ref. [52]
(0001)	0.58	0.64	−0.02	0.40	0.36	0.92	0.559, 0.573	0.54, 0.46
(1$\bar{1}$00)	1.70	1.71	0.39			2.41		
(2$\bar{1}\bar{1}$0)	1.22	1.25	0.19			1.88		

Figure 9. The phonon dispersion curves for Be_2C (CaF_2 structure) according to DFT calculations and the Be–C potential.

Table 8. DFT data and results using the potentials for H defects in Be. The formation energies are given in eV. The interstitial configurations are basal tetrahedral (BT) and octahedral (O). The ground state with the potentials is the tetrahedral (T) position.

	ABOP		DFT	
	Be–H I	Be–H II	Ref. [57]	Ref. [43]
Interstitials				
E_f^{BT}	1.22	1.35	0.8	1.58
E_f^O	1.46	1.71	Unstable	1.79
Ground state	1.04	1.17	0.8	1.58
BT to O migration barrier				
E_m	0.43	0.45		0.38

The potential parameters are presented in table 1 and a comparison with DFT data in tables 8 and 9. It could be possible to improve the potential by refitting the Be–Be potentials with Be–H in mind. This, however, puts limitations on the pure Be and Be–C potentials. Another option is to modify the potential formalism; however, as explained above it is preferable to keep the same formalism for all elements. The limited *ab initio* or experimental data available makes it difficult to benchmark a new formalism.

The diffusion of H in Be is described within the Be–H I potential by the equation $D = 3.3 \times 10^{-8} e^{-0.08\,eV/kT}$ m^2 s^{-1}. The ranges in the experimentally obtained prefactors D_0 and activation energies E_A are large; D_0 values from 6.7×10^{-9} to 9×10^{-12} m^2 s^{-1} and E_A values from 0.15 to 0.29 eV have been reported [4]. The potential thus overestimates the prefactor and underestimates the activation energy slightly.

Table 9. DFT data and results using the potentials for Be–H$_n$ molecules. The binding energies are given in eV and bond lengths in Å. Be–H$_3$ C2v breaks up into H$_2$ and Be with the potentials.

	ABOP		
	Be–H I	Be–H II	DFT [44]
Be–H			
E_c/atom	−1.30	−1.30	−1.30
r_b	1.34	1.34	1.34
Be–H$_2$ linear			
E_c/atom	−1.65	−1.61	−2.13
r_b	1.35	1.35	1.33
Be–H$_3$ D3h			
E_c/atom	−1.31	−1.46	−1.35
r_b	1.41	1.40	1.47
Be–H$_3$ C2v			
E_c/atom	—	—	−1.65
r_b	—	—	1.47
Angle	—	—	53°

4. Application of the beryllium potential

As an application of the Be potential, self-sputtering was studied. Simulations of Be ions with energies in the range 20–100 eV bombarding (0001) and ($\bar{1}\bar{1}20$) Be at normal incidence were performed. One thousand cumulative simulations, at a flux of 2.0×10^{28} m^{-2} s^{-1}, were done at each energy, and between every single bombardment the cell was shifted in x and y directions so as to model uniform bombardment of the surface. The temperature of the borders of the cell (consisting of 3388 atoms) was controlled to 320 K and the two bottommost layers were fixed to mimic an infinite lattice. After each bombardment, the cell was relaxed for 5 ps at 320 K.

Snapshots of the simulations are seen in figures 10(a)–(d), which illustrate 100 eV Be ions hitting (0001) Be. Defects are seen to form and migrate collectively to the surface and form an extra layer. This mechanism occurred several times during the simulations, therefore preventing amorphization. Thus, Be behaves as a typical metal which is hard to amorphize [59].

Regardless of the surface, no sputtering was seen at 20 eV and the yield is the same for both surfaces at 50 eV, indicating that the self-sputtering threshold lies between these two energies. At higher energies, bombardment of the ($\bar{1}\bar{1}20$) surface results in a higher yield (see figure 11), which is expected due to the larger distances between the ($\bar{1}\bar{1}20$) surface atoms. The sputtering results of Ueda *et al* [18] are also added to the figure, showing a similar picture.

To obtain experimental values that enable qualitative comparison, one has to extrapolate from results obtained with ion energies in the keV range and with polycrystalline samples [60]. What further hinders exact comparison is that the fluxes are a few orders of magnitude lower (typically $\sim 10^{20}$ m^{-2} s^{-1}) and that the temperatures are higher ($\sim$670 K) in the experiments [61–63]. The maximum observed sputtering yield, which is determined by a weight-loss method, is about 0.4 atoms/ion for ion energies of 1–5 keV. A downwards extrapolation of the experimental data points indicates a yield of 0.02–0.07 atoms/ion in the energy range 50–100 eV. This agrees well with our simulated values.
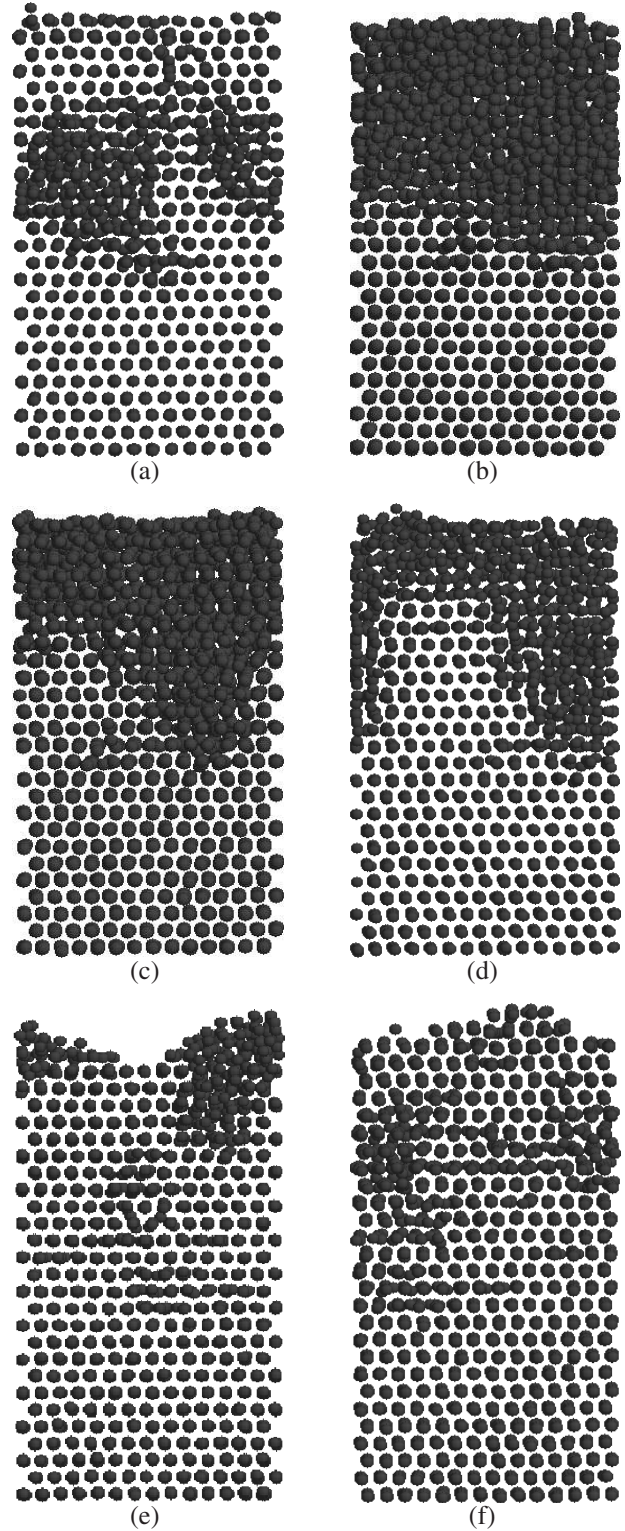

Figure 10. Snapshots of the beryllium self-bombardment. The incoming ion energies are 100 eV and the surface is (0001). The movement of defects to the surface is seen in (a)–(e) and the build up of extra surface layers is visible in (f).

A fit to the simulated values at low energies and to experimental ones at higher energies was done, as seen in figure 11. The $Y(E_0)$ formula of Eckstein *et al* [64] was used, with constants $E_{th} = 25$ eV, $q = 4.9$ $\mu = 1$ and $\lambda = 99$.
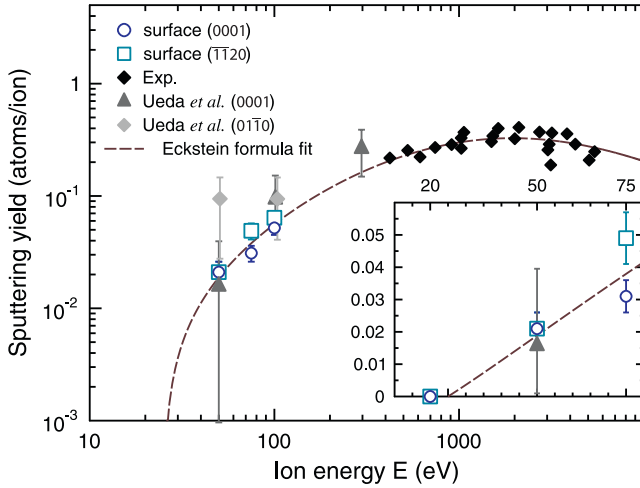
Figure 11. The sputtering yield of Be self-bombardment. Different surfaces result in different yields and the sputtering formula of Eckstein *et al* [64] is fitted to the simulated as well as to high energy experimental data [60]. The results of simulations by Ueda *et al* in [18] are also added for comparison. The inset shows the yield at low energies.

We also simulated the sputtering with the binary collision code TRIM [65], and looked at the resulting yield for different surface binding energies. For an energy of 3.32 eV, the simulated yields agreed well with the experimental ones, but in the lower ion energy range the yields were about three times larger than the values obtained with MD. Using a surface binding energy of 6 eV resulted in agreement on low ion energies, but at keV energies the yields were lower than the experimental values.

5. Conclusions

We have developed analytical bond-order potentials for Be–C–H systems. These potentials are suitable for studies in plasma–wall interactions in fusion reactors, since they are able to model non-equilibrium phenomena such as sputtering and the formation of mixed materials. The potentials were fitted to an extensive database consisting of DFT calculations of several structures as a complement to experimental data from the literature. The Brenner hydrocarbon potentials are used for the H–C interaction and two different Be potentials were parametrized. One (Be–Be I) describes the pure element and the other (Be–Be II) describes Be in Be–C. Both model the elemental equilibrium properties well, but the point defect energetics only fairly well, although the right stable interstitial configuration is reproduced when compared to DFT calculations. Be–Be I does also well in modelling the self-sputtering mechanism, showing a yield and threshold energy

that agrees with experiments. A Be–H potential for each Be–Be version was also parametrized, and these are able to model Be–H molecules as well as H defects and migration in Be. The only experimentally observed phase of Be–C is the ionic antifluorite Be_2C structure, which the Be–C potential captures well. A random melt with Be:C = 2:1 crystallizes into the Be_2C structure and regions of three-fold bonded C and Be_2C are formed when the ratio is 1:1.

Acknowledgments

Appendix A. Modification of the repulsive potential

The repulsive part of the potentials was modified in a manner previously used for Tersoff-like many-body potentials [66, 8, 67]: a total potential V_{Tot} was constructed by joining the original universal ZBL repulsive potential $V_{ZBL}(r)$ [68] with the equilibrium potential $V_{Eq}(r)$ using

$$V_{Tot}(r) = V_{ZBL}(r)(1 - F(r)) + V_{Eq}(r)F(r), \quad (A.1)$$

where V_{Eq} is the potential for states close to equilibrium described in the main text and the Fermi function

$$F(r) = \frac{1}{1 + e^{-b_f(r - r_f)}}. \quad (A.2)$$

Note that the Fermi function is used here merely as a function which smoothly goes from 1 to 0 in a relatively narrow r interval, with no connection to the Fermi level of the electrons of the solid. The values of the constants b_f and r_f are manually chosen so that the potential is essentially unmodified at the equilibrium and longer bonding distances, and that a smooth fit at short separations with no spurious minima is achieved for all realistic coordination numbers. The parameters for each potential are found in table A.1, where the parameters for C–C, C–H and H–H are those derived in [12].

Appendix B. Calculations of formation energies

The (free) energy/heat/enthalpy of formation of a substance $A_m B_n$ containing N_A (N_B) atoms of species A (B), with $N_A/N_B = m/n$, can be defined as

$$G_f = G_D - N_A g(A) - N_B g(B), \quad (B.1)$$

Table A.1. Parameters for the repulsive potentials. The C–C, H–H and C–H parameters are taken from [12].

	Be–Be I	Be–Be II	Be–C	Be–H I	Be–H II	C–C	H–H	C–H
r_f (Å)	0.8	0.8	0.7	0.8	0.8	0.6	0.35	0.5
b_f (1 Å^{-1})	7	15	16	15	15	8	15	10

when using the Gibbs free energy. Here G_D is the energy of the substance, $g(A)$ is the Gibbs energy per atom (in the reference state), also known as the chemical potential, $\mu(A) = g(A)$, and correspondingly for B. Usually G_f is normalized to the number N of formula units, which in this case equals $N = N_A/m = N_B/n$.

At $T = 0$ and standard 1 atm pressure $PV \approx 0$ and the Gibbs energy equals the internal potential energy. If the substance A_mB_n is formed from bulk elements the energy of formation becomes

$$G_f = G_D - N_A E_c(A) - N_B E_c(B), \qquad (B.2)$$

where $g = E_c$ is the cohesive energy. G_f is now the net energy cost of making A_mB_n from pure bulk elements. In the calculations of the heat of formation of Be_2C, the reference states of the bulk elements were graphite for C ($E_c^{C,gra} = -7.3768$ eV/atom [7]) and hcp for Be ($E_c^{Be,hcp} = -3.6234$ eV/atom).

Concerning defects, e.g. a vacancy, the formation energy is defined as in (B.1). However, there are some important differences. Consider a vacancy formed by removing one atom of element A which stays in the same system and does not enter an external particle reservoir of the pure element. Now G_D equals the energy of the cell with the vacancy, N_A (N_B) is the number of atoms of element A (B) in the defective cell, and $g(A)$ ($g(B)$) is the energy per atom of element A (B) in a cell containing perfect A_mB_n.

The cost of creating a vacancy of type A equals the energy difference between a defective cell and a perfect cell. To make sense physically, this defective cell containing a type A vacancy must also contain the removed A atom, either as an interstitial or as an adatom. However, taking these defects into account makes a simple definition of the energy of formation of a vacancy impossible, since the definition would at the same time include the energy of formation of an interstitial or an adatom.

Let us now summarize the energy of formation of a vacancy (vac.) and an interstitial (int.) of type A using the above recipe:

$$G_f^{A-vac.} = G_D^{A-vac.} - (N_A - 1)g(A) - N_B g(B), \qquad (B.3)$$

$$G_f^{A-int.} = G_D^{A-int.} - (N_A + 1)g(A) - N_B g(B). \qquad (B.4)$$

Here N_A is the number of atoms of type A in the perfect cell, and similarly for B. These equations are in line with the ideas in [69]. The sum of the two equations above is

$$G_f^{A-vac.} + G_f^{A-int.} = G_D^{A-vac.} + G_D^{A-int.} - 2N_A g(A)$$
$$- 2N_B g(B) \qquad (B.5)$$
$$= G_D^{A-vac.} + G_D^{A-int.} - 2G(A_mB_n). \qquad (B.6)$$

This is indeed the net energy cost of creating a type A vacancy and its associated interstitial, given as the energy difference between a defective cell and a perfect cell. In other words, the definition in (B.1) is consistent and physically meaningful, although this does not appear so at first.

In the calculation of a Be and C vacancy in Be_2C, a simulation cell containing 1500 atoms and one vacancy ($N_{Be} =$

$1000 = N_A$, $N_C = 500 = N_B$) was used. The pressure and temperature were controlled to 0 bar and 0 K, hence $g_A = g_{Be}$ and $g_B = g_C$ equals the potential energy of Be and C in perfect Be_2C, respectively. Here $g_{Be} = -5.414$ eV/atom and $g_C = -5.1861$ eV/atom.

References

[1] ITER Physics Basis Editors, ITER Physics Expert Group Chairs and Co-Chairs and ITER Joint Central Team and Physics Integration Unit 1999 ITER physics basis *Nucl. Fusion* **39** 2137–638
[2] Federici G 2006 Plasma wall interactions in ITER *Phys. Scr.* T **124** 1–8
[3] Barabash V, Federici G, Matera R, Raffray A R and ITER Home Teams 1999 *Phys. Scr.* T **81** 74–83
[4] Causey R A 2002 Hydrogen isotope retention and recycling in fusion reactor plasma-facing components *J. Nucl. Mater.* **300** 91
[5] Doerner R P, Baldwin M, Hanna J, Linsmeier C, Nishijima D, Pugno R, Roth J, Schmid K and Wiltner A 2007 Interaction of beryllium containing plasma with ITER materials *Phys. Scr.* T **128** 115–20
[6] Tersoff J 1988 New empirical approach for the structure and energy of covalent systems *Phys. Rev.* B **37** 6991
[7] Brenner D W 1990 Empirical potential for hydrocarbons for use in simulating the chemical vapor deposition of diamond films *Phys. Rev.* B **42** 9458
[8] Albe K, Nordlund K and Averback R S 2002 Modeling metal–semiconductor interaction: analytical bond-order potential for platinum–carbon *Phys. Rev.* B **65** 195124
[9] Nord J, Albe K, Erhart P and Nordlund K 2003 Modelling of compound semiconductors: analytical bond-order potential for gallium, nitrogen and gallium nitride *J. Phys.: Condens. Matter* **15** 5649–62
[10] Albe K, Nordlund K, Nord J and Kuronen A 2002 Modelling of compound semiconductors: analytical bond-order potential for Ga, As and GaAs *Phys. Rev.* B **66** 035205
[11] Erhart P and Albe K 2005 Analytic bond-order potential for atomistic simulations of silicon, carbon, and silicon carbide *Phys. Rev.* B **71** 035211
[12] Juslin N, Erhart P, Träskelin P, Nord J, Henriksson K O E, Nordlund K, Salonen E and Albe K 2005 Analytical interatomic potential for modelling non-equilibrium processes in the W–C–H system *J. Appl. Phys.* **98** 123520
[13] Müller M, Erhart P and Albe K 2007 Analytic bond-order potential for bcc and fcc iron—comparison with established eam potentials *J. Phys.: Condens. Matter* **19** 326220
[14] Blaisten-Barojas E and Khanna S N 1988 Development of a first-principles many-body potential for beryllium *Phys. Rev. Lett.* **61** 1477–80
[15] Igarashi M, Khanhta K and Vitek V 1991 N-body interatomic potentials for hexagonal close-packed metals *Phil. Mag.* B **62** 603–27
[16] Baskes M I and Johnson R A 1994 Modified embedded atom potentials for hcp metals *Modelling Simul. Mater. Sci. Eng.* **2** 147
[17] Hu W, Zhang B, Huang B, Gao F and Bacon D J 2001 Analytic modified embedded atom potentials for hcp metals *J. Phys.: Condens. Matter* **13** 1193–213
[18] Ueda S, Ohsaka T and Kuwajima S 1998 Molecular dynamics evaluation of self-sputtering of beryllium *J. Nucl. Mater.* **258–263** 713–8
[19] Brenner D W 1992 *Phys. Rev.* B **46** 1948
[20] Pauling L 1960 *The Nature of the Chemical Bond* 3rd edn (Ithaca: Cornell University Press)
[21] Cleri F and Rosato V 1993 Tight-binding potentials for transition metals and alloys *Phys. Rev.* B **48** 22

[22] Daw M S and Baskes M I 1984 Embedded-atom method: derivation and application to impurities, surfaces, and other defects in metals *Phys. Rev.* B **29** 6443–53

[23] Brenner D 1989 Relationship between the embedded-atom method and Tersoff potentials *Phys. Rev. Lett.* **63** 1022

[24] Blöchl P E 1994 Projector augmented-wave method *Phys. Rev.* B **50** 17953–79

[25] Kresse G and Hafner J 1993 *Ab initio* molecular dynamics for liquid metals *Phys. Rev.* B **47** 558–61

[26] Kresse G and Hafner J 1994 *Ab initio* molecular-dynamics simulation of the liquid-metal–amorphous-semiconductor transition in germanium *Phys. Rev.* B **49** 14251–69

[27] Kresse G and Furthmüller J 1996 Efficiency of *ab initio* total energy calculations for metals and semiconductors using a plane-wave basis set *Comput. Mater. Sci.* **6** 15–50

[28] Kresse G and Furthmüller J 1996 Efficient iterative schemes for *ab initio* total-energy calculations using a plane-wave basis set *Phys. Rev.* B **54** 11169–86

[29] Kresse G and Joubert D 1999 From ultrasoft pseudopotentials to the projector augmented-wave method *Phys. Rev.* B **59** 1758–75

[30] Perdew J P and Zunger A 1981 Self-interaction correction to density-functional approximations for many-electron systems *Phys. Rev.* B **23** 5048–79

[31] Perdew J P, Chevary J A, Vosko S H, Jackson K A, Pederson M R, Singh D J and Fiolhais C 1992 Atoms, molecules, solids, and surfaces: applications of the generalized gradient approximation for exchange and correlation *Phys. Rev.* B **46** 6671–87

[32] Wang Y and Perdew J P 1991 Correlation hole of the spin-polarized electron gas, with exact small-wavevector and high-density scaling *Phys. Rev.* B **44** 13298–307

[33] Monkhorst H J and Pack J D 1976 Special points for Brillouin-zone integrations *Phys. Rev.* B **13** 5188–92

[34] Blöchl P E, Jepsen O and Andersen O K 1994 Improved tetrahedron method for Brillouin-zone integrations *Phys. Rev.* B **49** 16223–33

[35] Alfè D, Program available at http://chianti.geol.ucl.ac.uk/~dario

[36] Petzow G, Aldinger F, Jonsson S and Preuss O 1985 *Ullmanns Encyclopedia of Industrial Chemistry* vol A4 (New York: VCH)

[37] Evans W J, Lipp M J, Cynn H, Yoo C S, Somayazulu M, Häusermann D, Shen G and Prakapenka V 2005 X-ray diffraction and Raman studies of beryllium: static and elastic properties at high pressures *Phys. Rev.* B **72** 094113

[38] Kádas K, Vitos L and Kollár J 2007 Structural stability of *beta*-beryllium *Phys. Rev.* B **75** 035132

[39] Sin'ko G V and Smirnov N A 2005 Relative stbaility and elastic properties of hcp, bcc, and fcc beryllium under pressure *Phys. Rev.* B **71** 214108

[40] Coobs J H and Koshuba W J 1952 The synthesis, fabrication, and properties of beryllium carbide *J. Electrochem. Soc.* **99** 15–120

[41] Albe K, Nord J and Nordlund K 2009 Dynamic charge-transfer bond-order potential for gallium nitride *Phil. Mag.* A at press

[42] Krimmel H and Fähnle M 1998 Hydrogen and vacancies in the tokamak plasma-facing material beryllium *J. Nucl. Mater.* **255** 72

[43] Ganchenkova M G, Vladimirov P V and Borodin V A 2008 Vacancies, interstitials and gas atoms in beryllium *J. Nucl. Mater.* at press

[44] Allouche A 2008 private communication

[45] Murray C W, Handy N C and Amos R D 1993 A study of O_3, S_3, CH_2, and Be_2 using Kohn-Sham theory with accurate quadrature and large basis set *J. Chem. Phys.* **98** 7145

[46] Weiner B and Öhrn Y 1985 Calculation of spectroscopic properties of the ground and excited states of Be_2 according to the antisymmetrized gemial power (AGP) based excitation propagator *J. Chem. Phys.* **83** 6

[47] Morris J R, Wang C Z, Ho K M and Chan C T 1994 Melting line of aluminum from simulations of coexisting phases *Phys. Rev.* B **49** 3109

[48] Nakano K, Akahama Y and Kawamura H 2002 X-ray diffraction study of Be to megabar pressure *J. Phys.: Condens. Matter* **14** 10569–73

[49] Wise J L, Chhabildas L C and Asay J R 1982 Shock compression of beryllium *AIP Conf. Proc.* **78** 417–21

[50] Meyerhoff R W and Smith J F 1962 Anisotropic thermal expansion of single crystals of thallium, yttrium, beryllium, and zinc at low temperatures *J. Appl. Phys.* **33** 219

[51] Ganchenkova M G and Borodin V A 2007 *Ab initio* study of small vacancy complexes in beryllium *Phys. Rev.* B **75** 05418

[52] Wachowicz E and Kiejna A 2001 Bulk and surface properties of hexagonal-close-packed Be and Mg *J. Phys.: Condens. Matter* **13** 10767–76

[53] Stedman R, Amilius Z, Pauli R and Sundin O 1976 *J. Phys. F: Met. Phys.* **6** 157

[54] Rinehart G H and Behrens R G 1980 Vapor pressure and thermodynamics of beryllium carbide *J. Chem. Thermodyn.* **12** 835–42

[55] Weast R C and Astle M J 1982 *CRC Handbook of Chemistry and Physics* 63rd edn (Boca Raton, FL: CRC Press)

[56] Beaver W W 1955 *The Metal Beryllium* (Cleveland, OH: American Society for Metals) chapter XI (Refractory Compounds and Cermets of Beryllium) pp 570–98

[57] Krimmel H and Fähnle M 1996 Properties of hydrogen isotopes in the tokamak plasma-facing material beryllium *J. Nucl. Mater.* **231** 159

[58] Swansiger WA 1986 *J. Vac. Sci. Technol.* A **4** 1216

[59] Averback R S and Diaz de la Rubia T 1998 Displacement damage in irradiated metals and semiconductors *Solid State Physics* vol 51, ed H Ehrenfest and F Spaepen (New York: Academic) pp 281–402

[60] Behrisch R and Eckstein W (ed) 2007 *Sputtering by Particle Bombardment: Experiments and Computer Calculations from Threshold to MeV Energies* (Berlin: Springer)

[61] Guseva M, Gureev V, Korshunov S, Neumoin V, Sokolov Y, Stolyarova V, Vasiliev V, Rylov S and Strunnikov V 1995 Selfsputtering of beryllium and sputtering and erosion of C–C composite in the experiments on plasma disrution simulation *J. Nucl. Mater.* **220–222** 957–60

[62] Guseva M, Birukov A, Gureev V, Daneljan L, Korshunov S, Martynenko Y, Moskovkin P, Sokolov Y, Stoljarova V, Kulikauskas V and Zatekin V 1996 Investigation of the beryllium ion-surface interaction *J. Nucl. Mater.* **233–237** 681–7

[63] Guseva M, Korshunov S, Gureev V, Martinenko Y, Neumoin V and Stoljarova V 1997 Investigation of beryllium self-sputtering *J. Nucl. Mater.* **241** 1117–21

[64] Eckstein W and Preuss R 2003 New fit formulae for the sputtering yield *J. Nucl. Mater.* **320** 209–13

[65] Ziegler J F, SRIM-2008 software package available online at http://www.srim.org

[66] Nordlund K, Keinonen J and Mattila T 1996 Formation of ion irradiation-induced small-scale defects on graphite surfaces *Phys. Rev. Lett.* **77** 699

[67] Björkas C and Nordlund K 2007 Comparative study of cascade damage in Fe simulated with recent potentials *Nucl. Instrum. Methods Phys. Res.* B **259** 853–60

[68] Ziegler J F, Biersack J P and Littmark U 1985 *The Stopping and Range of Ions in Matter* (New York: Pergamon)

[69] Qian G-X, Martin R M and Chadi D J 1988 First-principles study of the atomic reconstruction and energies of Ga- and As-stabilized GaAs(100) surfaces *Phys. Rev.* B **38** 7649

[70] Bondybey V E and English J H 1984 Laser vaporization of beryllium: gas phase spectrum and molecular potential of Be_2 *J. Chem. Phys.* **80** 568–70

[71] Lide D R 2001 *CRC Handbook of Chemistry and Physics* 82nd edn (Boca Raton, FL: CRC Press)

[72] Kittel C 1968 *Introduction to Solid State Physics* 3rd edn (New York: Wiley)

[73] Chou M Y, Lam P K and Cohen M L 1983 *Ab initio* study of structural and electronic properties of beryllium *Phys. Rev.* B **28** 4179–85

[74] Migliori A, Ledbetter H, Thoma D J and Darling T W 2004 Beryllium's monocrystal and polycrystal elastic constants *J. Appl. Phys.* **95** 2436–40

[75] Silversmith D J and Averbach B L 1970 Pressure dependence of the elastic constants of beryllium and beryllium–copper alloys *Phys. Rev.* B **1** 567–71

[76] Lee C H, Lambrecht W R L and Segall B 1995 Electronic structure of Be_2C *Phys. Rev.* B **51** 10392

[77] Laref S and Laref A 2008 Mechanical, electronic and optical properties of antifluorites semiconductors X_2C ($x = Mg$, Be) *Comput. Mater. Sci.* **44** 664–9

[78] Disko M M, Spence J C H, Sankey O F and Saldin D 1986 Electron-energy-loss near-edge structure of Be_2C *Phys. Rev.* B **33** 5642

[79] Staritzky E 1956 *Anal. Chem.* **28** 915

[80] Barnes W P 1966 Considerations in the use of beryllium for mirrors *Appl. Opt.* **5** 1883

[81] Holzwarth N A W and Zeng Y 1995 Density-functional calculation of the bulk and surface geometry of beryllium *Phys. Rev.* B **51** 13653–9